Accepted Manuscript

A multi-cracked particle method for complex fracture problems in 2D

Weilong Ai, Charles E. Augarde

Please cite this article as: W. Ai, C.E. Augarde, A multi-cracked particle method for complex fracture problems in 2D, *Math. Comput. Simulation* (2018), https://doi.org/10.1016/j.matcom.2018.02.005
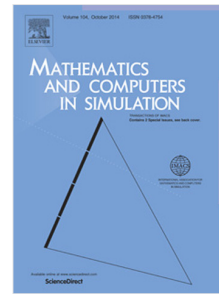
A multi-cracked particle method for complex fracture problems in 2D

Weilong Ai[a,*], Charles E. Augarde[a]

[a]*Department of Engineering, Durham University, South Road, Durham, DH1 3LE, UK*

Abstract

Practical fracture problems are characterised by complex patterns of multiple and branching cracks, somewhat far removed from the fracture problems used for validation of numerical methods, involving single cracks, and the simulation of complex multi-tipped cracks brings many challenges to current numerical methods. The cracking particle method (CPM) incorporates the description of a crack path into the meshless nodes or particles used to discretise a domain. The CPM has recently been improved to make the crack paths continuous and to include adaptivity. In this paper we take this improved CPM further and introduce new crack particles which can model multiple fractures to handle crack branches and crack junctions without the need for any specialised techniques such as enrichment. Some examples with complex crack patterns are tested to show the performance of the proposed methodology and good results are obtained which agree well with previous papers.

Keywords: Cracking particle method, meshless, multiple cracks, adaptivity

1. Introduction

Fracture is a common phenomenon affecting materials such as soil, bone and concrete, however theoretical work to study this problem is difficult to carry out since fracture is a highly non-linear behaviour. In recent decades, several numerical methods have been used for fracture simulation, such as the finite element method (FEM) [33, 46, 52], the extended FEM (XFEM) [6, 18], the element-free Galerkin method (EFGM) [9–11], the numerical manifold method (NMM) [27, 40, 48] and the cracking particle method (CPM) [35, 38, 39], and many good predictions have been obtained for standard test cases [8, 31]. However, there are limitations to the use of some of these numerical methods when applied to more complex examples. Specifically, in the FEM, a crack path is confined to mesh edges perhaps with the use of interface elements [46]. In the XFEM and the EFGM, an explicit description of the crack path is required, which is usually fulfilled using level set functions, and when the number of cracks increases, the expense of updating the level set functions becomes very high [17, 50]. In the NMM, the discontinuities along crack paths are handled by dividing the problem domain into "mathematical covers" and "physical covers", but

---

*Corresponding author
Email address: `weilong.ai@durham.ac.uk` (Weilong Ai)

the generation of these covers is currently a bottleneck of this approach [14]. The phase field approach for fracture modelling has been developed recently [2, 28, 29, 44], where crack propagation is handled by a scalar field independent of the main discretisation (meshed or not), and the complexity of tracking crack geometries is not required, although the evolution of the phase field during crack propagation brings an extra calculation burden often making the method not computationally cheap. In the CPM, crack paths are simulated by a set of cracking particles with discontinuous crack segments, as shown in Fig. 1 and it is easy to update crack patterns by adding or deleting cracking particles, which makes it a suitable candidate for complex fracture modelling [35, 38].

The CPM was first proposed by Rabczuk in 2004 [35], where the discontinuity at crack paths was achieved by extra enrichments. It was later shown that these enrichments can be removed by splitting the cracking particles into two new particles [39]. This CPM has been applied to static fracture [37], dynamic fracture [24, 25] and ductile fracture [23]. There are also some papers using cracking-particle-type methods for fracture modelling [15, 49]. Some integration issues are discussed in [45] and instabilities are avoided by using stabilized nodal integration. The original CPM suffers from spurious cracking, as mentioned in [39, 45], but this is addressed in [1] via a modified CPM using a bilinear cracking segment approach where the cracking angle can be recorded using two crack branches so that more accurate curvature of crack paths can be modelled. That paper also introduced an adaptivity scheme for use with the method. The CPM has already been applied in 3D crack problems [38, 39], but spurious crack results were found due to simple assumptions in the method, i.e. using a set of planar discontinuous segments to approximate 3D non-planar crack surfaces. Possible solutions to this issue are to use level sets [22, 51] or triangular meshes [4, 19]. Although level sets can provide an accurate crack description, updating these functions is time consuming [51], while triangular meshes can explicitly describe crack propagation with low cost [20]. This part of work is currently under development by the authors.

Here we describe a further development of the modified CPM which can deal with branched cracks by splitting a cracking particle multiply. The paper is organized as follows: firstly, governing equations of the modified CPM are presented. Then the description of the discontinuity at a crack path using the CPM is demonstrated showing how it can be adapted for a branched crack. The adaptivity scheme of [1] is also improved to deal with branched cracks. Some numerical examples are included to illustrate the features of the modified CPM for complex fracture patterns.

2. Governing equations

Considering a two dimensional (2D) problem with domain Ω and boundary Γ, the equilibrium equation (strong form) is

$$\nabla \cdot \boldsymbol{\sigma} + \mathbf{b} = \mathbf{0} \qquad \text{in } \Omega, \tag{1}$$

and the boundary conditions are

$$\boldsymbol{\sigma} \cdot \mathbf{n} = \bar{\mathbf{t}} \qquad \text{on } \Gamma_t \,, \tag{2}$$

$$\mathbf{u} = \bar{\mathbf{u}} \qquad \text{on } \Gamma_u \,, \tag{3}$$

where $\boldsymbol{\sigma}$ is the Cauchy stress tensor, $\mathbf{b}$ is the body force vector (if present), $\mathbf{n}$ is the unit normal to the domain Ω and $\mathbf{u}$ is the displacement vector. $\bar{\mathbf{t}}$ and $\bar{\mathbf{u}}$ are traction and displacement constraints respectively on the boundary Γ with $\Gamma = \Gamma_t \bigcup \Gamma_u$. However, for realistic problems a weak form (under the principle of virtual work for instance) is applied alternatively as below and then discretised in the CPM using the EFGM

$$\int_\Omega \nabla_s \delta \mathbf{v} : \boldsymbol{\sigma} \mathrm{d}\Omega = \int_\Omega \delta \mathbf{v} \cdot \mathbf{b} \mathrm{d}\Omega + \int_{\Gamma_t} \delta \mathbf{v} \cdot \bar{\mathbf{t}} \mathrm{d}\Gamma \,. \tag{4}$$

where ":" is the double dot product of tensors.

Trial functions for the weak form discretised using the EFGM are constructed via a moving least squares (MLS) approximation since the approach is meshless and the approximated displacement is

$$u^h(\mathbf{x}) = \sum_I^n \Phi_I(\mathbf{x}) u_I = \boldsymbol{\Phi}^{\mathrm{T}} \mathbf{u} \,, \tag{5}$$

and the shape functions Φ_I are

$$\boldsymbol{\Phi}(\mathbf{x}) = \mathbf{p}^{\mathrm{T}}(\mathbf{x}) \mathbf{A}(\mathbf{x})^{-1} \mathbf{B}(\mathbf{x}) \,, \tag{6}$$

where

$$\mathbf{A}(\mathbf{x}) = \sum_I^n w_I(\mathbf{x} - \mathbf{x}_I) \mathbf{p}^{\mathrm{T}}(\mathbf{x}_I) \mathbf{p}(\mathbf{x}_I) \,, \tag{7}$$

and

$$\mathbf{B}(\mathbf{x}) = [w_1(\mathbf{x} - \mathbf{x}_1) \mathbf{p}(\mathbf{x}_1), w_2(\mathbf{x} - \mathbf{x}_2) \mathbf{p}(\mathbf{x}_2), ..., w_n(\mathbf{x} - \mathbf{x}_n) \mathbf{p}(\mathbf{x}_n)] \,. \tag{8}$$

The weight functions w_I can be chosen to follow many EFGM references, e.g. [7, 9, 21] and the function used here (4th order spline function) is

$$w_I(\mathbf{x} - \mathbf{x}_I) = w_I(s) = \begin{cases} 1 - 6s^2 + 8s^3 - 3s^4 & \text{if } s \le 1 \\ 0 & \text{if } s > 1 \,, \end{cases} \tag{9}$$

where s is the ratio between the distance of $\mathbf{x}$ and $\mathbf{x}_I$ and the support size (also known as the dilatation parameter) of node I.

3. Crack description

In meshless methods, there are two main approaches to describe the discontinuity at a crack: the visibility criterion [9] and the diffraction criterion [32]. In the former approach, the influenced domain (support) of a node is modified by deleting the part that is "shadowed" by the presence of the discontinuity. A problem is the continuity of resulting shape functions that are not even C_0 continuous, and the approach can suffer from large errors and oscillations at crack tips for large dilatation parameters [32]. In the diffraction criterion, a diffraction zone of the rays around a crack tip is considered and more accurate approximations around the crack tip can be obtained [16, 32]. But, when the number of cracks increases, the expense of defining diffraction zones becomes high. Some contributions, e.g. [5, 30, 41] tackle this issue using weight functions for nodes which are modified around crack tips to improve accuracy, however here we are mainly concerned with discontinuity modelling at crack junctions and branches. For simplicity, therefore the visibility criterion is used rather than the diffraction criterion.

3.1. Complexities in the description of multiple cracks

The XFEM is one of the most popular methods for fracture modelling since the description of crack paths is not linked to meshes, and remeshing is totally avoided [13]. However, the XFEM becomes cumbersome for handling discontinuities of multiple and complex branching cracks. An example of a cross crack is now used to illustrate this issue.

The displacement in the standard XFEM is approximated by extra enrichments based on a partition of unity approach as

$$u^h(\mathbf{x}) = \sum_I^n \Phi_I(\mathbf{x}) u_I + \sum_I^{n_1} \Phi_I(\mathbf{x}) H(\mathbf{x}) b_I + \sum_I^{n_c} \Phi_I(\mathbf{x}) \left(\sum_{k=1}^4 R_k a_I^k \right) , \tag{10}$$

where $H(\mathbf{x})$ is the Heaviside function with values +1 for nodes on one side of the crack surface and -1 on the other side. n_1 is a group of nodes with support totally cut by the crack, while n_c is the set of nodes with supports containing the crack tip. b_I and a_I are nodal enrichment unknowns and R_k are near-tip enrichments and components of a vector as follows

$$\boldsymbol{R}(r,\theta) = \left[\sqrt{r}\sin(\frac{\theta}{2}), \sqrt{r}\cos(\frac{\theta}{2}), \sqrt{r}\sin(\theta)\sin(\frac{\theta}{2}), \sqrt{r}\sin(\theta)\cos(\frac{\theta}{2}) \right] , \tag{11}$$

where r and θ are local polar coordinates at the crack tip. When two or more intersecting cracks (e.g.

Fig. 2) are considered, the displacement field [3, 13, 17] becomes

$$u^h(\mathbf{x}) = \sum_I^n \Phi_I(\mathbf{x})u_I + \sum_I^{n_1} \Phi_I(\mathbf{x})H_1(\mathbf{x})b_{1I} + \sum_I^{n_2} \Phi_I(\mathbf{x})H_2(\mathbf{x})b_{2I}$$
$$+ \sum_I^{n_3} \Phi_I(\mathbf{x})H_3(\mathbf{x})b_{3I} + \sum_I^{n_{1,2}} \Phi_I(\mathbf{x})J_{1,2}(\mathbf{x})c_I+ \qquad (12)$$
$$\sum_I^{n_{1,3}} \Phi_I(\mathbf{x})J_{1,3}(\mathbf{x})d_I + \sum_I^{n_c} \Phi_I(\mathbf{x})\left(\sum_{k=1}^4 R_k a_I^k\right).$$

In the equation above, the subscripts of $H(\mathbf{x})$ and n indicate cracks 1 , 2 and 3, and $n_{1,2}$ is a set of nodes with supports containing the junction of cracks 1 and 2, similar to $n_{1,3}$ for cracks 1 and 3. $J_{1,2}(\mathbf{x})$ and $J_{1,3}(\mathbf{x})$ are two modified Heaviside functions with an extra value of 0 for the crack junctions, as shown in Fig. 2. b_{1I}, b_{2I}, b_{3I}, c_I, d_I and a_I are nodal enrichment unknowns. When the number of cracks increases, more enrichment terms are introduced and the computational cost rises.

For numerical methods (e.g. the XFEM and the EFGM) using a level set approach for the description of crack patterns, the number of level set functions will increase linearly with the number of cracks, as in [50], which also makes the simulation more complex. Even though it has been claimed that the NMM provides a simpler way for displacement approximation, as in [3], the cost for generating physical covers still hinders its application [14].

3.2. A simple approach to model multiple cracks using a CPM

In the CPM, crack paths are described by a set of cracking particles with discontinuous segments, and crack geometries are obtained as their connection. With the use of bilinear crack segments, as in [1] continuous crack paths are obtained and spurious cracking is avoided. In contrast to the methods described above, it is relatively easy to develop a multiple-split cracking particle method to represent complex crack patterns, and that is the crux of this paper. The method works as follows. For a cross crack, such as in Fig. 3, the junction node D is split into 4 nodes D_1, D_2, D_3 and D_4 and its support is also divided into 4 parts. The 4 nodes are not connected to each other and the crack opening at the junction point is achieved by the relative displacements of nodes D_1, D_2, D_3 and D_4. The displacement approximation is kept the same as Eq. 5 and the crack opening, marked as $[\![u(\mathbf{x})]\!]$, is

$$[\![u(\mathbf{x})]\!] = \sum_{I \in \mathcal{S}^+} \Phi_I(\mathbf{x}^+)u_I + \sum_{I \in \mathcal{S}^-} \Phi_I(\mathbf{x}^-)u_I, \qquad (13)$$

where $\mathbf{x}^+$ and $\mathbf{x}^-$ are two sets of nodes located on opposite sides of crack surfaces $\mathcal{S}^+$ and $\mathcal{S}^-$ respectively.

The discontinuities along crack surfaces are captured by modifying the support domain in the CPM rather than by using complex enrichment functions as in the XFEM. The visibility criterion (with the

algorithm from [34]) is used to describe the connection among normal particles. When cracking particles are involved, a simple strategy is used to distinguish these particles. The location of a cracking particle i is given a small shift at the bisector direction θ_i of its sector support, Eq. (14), then the standard visibility algorithm is used.

$$\begin{cases} x_i' = x_i + 0.0001 r_i \cos(\theta_i) \\ y_i' = y_i + 0.0001 r_i \sin(\theta_i) \,, \end{cases} \tag{14}$$

where r_i is the support size, (x_i, y_i) is the location of node i and (x_i', y_i') is the shifted location. With this strategy, four particles in the Fig. 3 (b) with the same location at the original particle D are shifted in different directions, Fig. 4, and it is easy to assess visibility between nodes i and D_1 while the other three nodes are not visible to node i. Note that the shift is only used in the visibility algorithm and the original location is used in the solution using the EFGM. The whole process is described in Algorithm 1.

Algorithm 1 Check the visibility between particles i and j

Input: Node information of nodes i and j
Output: *status*: 0 – invisible; 1 – visible
  $status \leftarrow 1$
  if node j is outside the support of node i **then**
    $status \leftarrow 0$
  else
    if node i is a cracking particle **then**
      shift the location of node i by Eq. (14)
    end if
    if node j is a cracking particle **then**
      shift the location of node j by Eq. (14)
    end if
    $status \leftarrow$ standard visibility criterion
  end if
  return *status*

3.3. Crack propagation criteria

A comparison among different criteria for the crack propagation can be found in [12], and of those, the maximum principal stress criterion maintains both efficiency and reasonable accuracy and is applied here. Stress intensity factors (SIFs) are calculated by the interaction integral method [47],

$$I = \int_A (\sigma_{ij}^{\mathrm{aux}} u_{j,1} + \sigma_{ij} u_{j,1}^{\mathrm{aux}} - \sigma_{jk}^{\mathrm{aux}} \varepsilon_{jk} \delta_{1i}) q_{,i}\, \mathrm{d}A, \quad i,j,k \in [1,2], \tag{15}$$

where q is a weight function with value 1 at the crack tip and 0 at the integration domain boundaries, the superscript "aux" indicates an auxiliary state which is initially predefined as in [47]. I is the interaction

integral having the following relationship with SIFs,

$$I = 2\alpha(K_{\mathrm{I}}K_{\mathrm{I}}^{\mathrm{aux}} + K_{\mathrm{II}}K_{\mathrm{II}}^{\mathrm{aux}}), \tag{16}$$

and

$$\alpha = \begin{cases} (1 - \nu^2)/E & \text{for plane strain}, \\ 1/E & \text{for plane stress}, \end{cases} \tag{17}$$

where E is the Young's modulus and ν is the Poisson's ratio. By choosing different auxiliary fields, SIFs can be obtained accordingly, e.g. set $K_{\mathrm{I}}^{\mathrm{aux}} = 1, K_{\mathrm{II}}^{\mathrm{aux}} = 0$ to get $K_{\mathrm{I}} = I/(2\alpha)$. The crack propagation angle θ_c is defined by setting the shear stress $\sigma_{r\theta}$ in a local polar coordinate system to zero following the maximum principal stress criterion,

$$\sigma_{r\theta} = \frac{1}{2\pi r} \cos(\theta/2)[\frac{1}{2}K_{\mathrm{I}}\sin(\theta) + \frac{1}{2}K_{\mathrm{II}}(3\cos(\theta) - 1)] = 0. \tag{18}$$

The solution is

$$\theta_c = 2\arctan(\frac{K_{\mathrm{I}} - \sqrt{K_{\mathrm{I}}^2 + 8K_{\mathrm{II}}^2}}{4K_{\mathrm{II}}}). \tag{19}$$

These features required for numerical modelling of linear elastic fracture mechanics are covered in many references [1, 6, 12].

4. Adaptivity

In the original CPM [35], a large number of nodes are required to obtain acceptable results, and it has been shown that this problem can be alleviated by introducing an adaptivity strategy [36, 38]. Coarse node arrangements can be set up at the beginning of an analysis and during the crack propagation process, fine arrangements can be generated automatically around crack tips to fulfil the accuracy requirement. There are difficulties with some adaptive schemes (e.g. [38]) where reconstruction of Voronoi cells is required during adaptive steps, which leads to an increase of computational cost. Since the EFGM requires a structured background grid of integration cells, it is convenient to base a refinement strategy on this as well [36, 42], by dividing a cell into four sub-cells. A recovery strategy (to coarsen node arrangements) proposed by Lee et al. [26] can further reduce the number of nodes, in which sub-cells are combined together again.

Here we base the adaptive strategy on a quadtree structure. Cells with large errors are divided into four sub-cells by a refinement approach, while a recovery function is used to combine sub-cells with small errors together to the original cell. The procedure is quite simple and illustrated in Fig. 5, where a background cell (numbered 1) with a large error is divided to four smaller cells (numbered 1, 2, 3, 4),

where the small cell 1 inherits the original cell number, and five new particles (in white) are added which are defined with half the support size of the particles in black. Then the support sizes of the four particles that occupied the original cell 1 are reduced in size and multiplied by $\sqrt[4]{0.5}$, which makes their support match the density of surrounding particles. The recovery process is the reverse of the refinement with five particles deleted as indicated in the Figure. A more detailed description of the procedure is given in an earlier paper [1]. It is notable that although uniform cells are depicted in Fig. 5, the adaptive strategy here is also applicable for methods using non-uniform cells. A recovery-based error estimator for the EFGM described in [16] is used, which is the energy norm of the difference between the calculated stress $\boldsymbol{\sigma}^h$ and the "projected" stresses $\boldsymbol{\sigma}^p$ (to approximate exact stresses) over the problem domain Ω as below

$$\|E_g\| = \left\{ \frac{1}{2} \int_\Omega (\boldsymbol{\sigma}^p - \boldsymbol{\sigma}^h)^{\mathrm{T}} \mathbf{D}^{-1} (\boldsymbol{\sigma}^p - \boldsymbol{\sigma}^h) \mathrm{d}\Omega \right\}^{1/2}, \tag{20}$$

where $\boldsymbol{\sigma}^p$ and $\boldsymbol{\sigma}^h$ are written in the Voigt notation, e.g. $\boldsymbol{\sigma}^p = [\sigma^p_{xx}, \sigma^p_{yy}, \sigma^p_{xy}]^{\mathrm{T}}$ and

$$\mathbf{D} = \frac{E}{1-\nu^2} \begin{bmatrix} 1 & \nu & 0 \\ \nu & 1 & 0 \\ 0 & 0 & \frac{(1-\nu)}{2} \end{bmatrix} \quad \text{for plane stress.} \tag{21}$$

$\boldsymbol{\sigma}^p$ is evaluated by an approximation at a point $\mathbf{x}$ with smaller supports

$$\boldsymbol{\sigma}^p(\mathbf{x}) = \sum_{k=1}^m \Psi_k(\mathbf{x}) \boldsymbol{\sigma}^h(\mathbf{x}_k), \tag{22}$$

where m is the total number of surrounding nodes $\mathbf{x}_k$ with supports covering the point $\mathbf{x}$, $\Psi_k(\mathbf{x})$ are shape functions obtained through the MLS scheme but with smaller supports. The normalized global error η_{g} is defined with

$$\eta_{\mathrm{g}} = \frac{\|E\|}{\|U\|}, \tag{23}$$

$$\|U\| = \left\{ \frac{1}{2} \int_\Omega (\boldsymbol{\sigma}^h)^{\mathrm{T}} \mathbf{D}^{-1} \boldsymbol{\sigma}^h \mathrm{d}\Omega \right\}^{1/2}. \tag{24}$$

The local error for a background cell i is evaluated by integrating over the local domain Ω_i

$$\|E_i\| = \left\{ \frac{1}{2} \int_{\Omega_i} (\boldsymbol{\sigma}^p - \boldsymbol{\sigma}^h)^{\mathrm{T}} \mathbf{D}^{-1} (\boldsymbol{\sigma}^p - \boldsymbol{\sigma}^h) \mathrm{d}\Omega_i \right\}^{1/2}. \tag{25}$$

$$\eta_i = \frac{\|E_i\|}{\|U\| / \sqrt{n_{\mathrm{cell}}}}, \tag{26}$$

with n_{cell} the total number of cells. The refinement and recovery are driven by the local error of a

8

background cell, i.e.

$$
\begin{cases}
\eta_i > L_{\text{fin}} & \text{to be refined}, \\
\eta_i < L_{\text{rec}} & \text{to be recovered},
\end{cases}
\tag{27}
$$

where L_{fin} is the refinement trigger and L_{rec} is the recovery trigger. To make the global error lower than the user defined target error η_{t} with the adaptivity, the following relationship from [1] is applied,

$$
L_{\text{fin}} = 2\eta_t, \; L_{\text{rec}} = 0.5\eta_t.
\tag{28}
$$

5. Numerical examples

To demonstrate the performance of the modified CPM for complex crack simulation, five 2D crack problems have been tested as below. Plane stress conditions with elastic material properties $E = 200\text{GPa}$ and $v = 0.3$ are used unless stated otherwise. In all examples, SIFs in the presentation of results are normalized by

$$
F_{\text{I}} = K_{\text{I}}/(\sigma\sqrt{\pi a}), \quad F_{\text{II}} = K_{\text{II}}/(\tau\sqrt{\pi a}).
\tag{29}
$$

5.1. A single crack under mixed mode loading

In this problem the behaviour of a single edge crack in a stress field which induces mixed mode fracture is modelled. The problem domain is a square of side length $w = 100$ mm where the crack is of length $a = 0.5w$ as in Fig. 6. This problem is extracted from that of a central crack in an infinite plate under biaxial tension $\sigma = 100\text{N/mm}$ and shear $\tau = 100\text{N/mm}$, where theoretical SIFs are $K_{\text{I}} = \sigma\sqrt{\pi a}$ and $K_{\text{II}} = \tau\sqrt{\pi a}$. The target error in the adaptivity is $\eta_{\text{t}} = 0.02$. The analytical solutions for the near-tip field are from Westergaard [43], i.e.

$$
\begin{cases}
\sigma_{xx} = \frac{K_{\text{I}}}{\sqrt{2\pi r}}\cos(\theta/2)[1 - \sin(\theta/2)\sin(3\theta/2)] - \frac{K_{\text{II}}}{\sqrt{2\pi r}}\sin(\theta/2)[2 + \cos(\theta/2)\cos(3\theta/2)], \\
\sigma_{yy} = \frac{K_{\text{I}}}{\sqrt{2\pi r}}\cos(\theta/2)[1 + \sin(\theta/2)\sin(3\theta/2)] + \frac{K_{\text{II}}}{\sqrt{2\pi r}}\sin(\theta/2)\cos(\theta/2)\cos(3\theta/2), \\
\sigma_{xy} = \frac{K_{\text{I}}}{\sqrt{2\pi r}}\cos(\theta/2)\sin(\theta/2)\cos(3\theta/2) + \frac{K_{\text{II}}}{\sqrt{2\pi r}}\cos(\theta/2)[1 - \sin(\theta/2)\sin(3\theta/2)], \\
u_x = \frac{K_{\text{I}}}{2\mu}\sqrt{\frac{r}{2\pi}}\cos(\theta/2)[\kappa - 1 + 2\sin^2(\theta/2)] + \frac{K_{\text{II}}}{2\mu}\sqrt{\frac{r}{2\pi}}\sin(\theta/2)[\kappa + 1 + 2\cos^2(\theta/2)], \\
u_y = \frac{K_{\text{I}}}{2\mu}\sqrt{\frac{r}{2\pi}}\sin(\theta/2)[\kappa + 1 - 2\cos^2(\theta/2)] - \frac{K_{\text{II}}}{2\mu}\sqrt{\frac{r}{2\pi}}\cos(\theta/2)[\kappa - 1 - 2\sin^2(\theta/2)],
\end{cases}
\tag{30}
$$

where μ and κ are material constants, as

$$
\mu = \frac{E}{2(1 + \nu)}, \quad \kappa = (3 - \nu)/(1 + \nu) \quad \text{for plane stress}
\tag{31}
$$

9

The analytical stresses are used as external loading as

$$\boldsymbol{f} = \boldsymbol{\sigma} \cdot \boldsymbol{n} = \begin{bmatrix} \sigma_{xx}n_x + \sigma_{xy}n_y \\ \sigma_{xy}n_x + \sigma_{yy}n_y \end{bmatrix}, \tag{32}$$

where $\boldsymbol{n} = [n_x, n_y]$ is the outer normal of each edge. The plate is fixed by setting as essential boundary conditions

$$\begin{aligned} u_x = 0, u_y = 0 \quad &\text{at } x = w/2, y = w/2, \\ u_y^+ + u_y^- = 0 \quad &\text{at } x = 0, y = w/2, \end{aligned} \tag{33}$$

where superscripts $^+$ and $^-$ stand for the two sides of the crack as in Eq (13).

A uniform distribution of nodes in Fig. 6 (b) is applied initially and subsequent adaptive particle distributions can be seen in Fig. 7. From Fig. 8 (a), projected errors by Eq (20) are similar with analytical errors where analytical stresses in Eq (30) are used. During adaptive steps, the predicted two mode SIFs approach the exact values as shown in Fig. 8 (b). The deformations of two crack surfaces are shown in Fig. 9, where both u_x and u_y can be seen to match the analytical solutions from Eq (30). A comparison between adaptive and uniform refinements is given in Table 1, where it is clear that adaptivity provides better accuracy for fewer particles and hence has a lower computational cost than uniform refinement, although it should be noted that adaptivity requires an overhead for adaptive steps. The calculating time is normalized by dividing the calculating time t_0 for the initial particle arrangement, i.e. time/t_0, where $t_0 = 18.123$s for running with MATLAB on a PC (i7 4790, 16GB RAM).

5.2. Edge crack

The crack propagation of an edge crack in a plate under shear loading is studied in this second example, and crack growth predictions which are calculated with different initial node arrangements are compared. The geometry of the problem is depicted in Fig. 10, where the plate has width $w = 70$mm and height $h = 160$mm and the crack length $a = 0.5w$, as in [26]. The lower edge of the plate is fixed and the upper edge is under a shear $\boldsymbol{\tau} = 100$N/mm. Three different particle arrangements are set initially, as in Fig. 10 (b-d). The material properties are $E = 206.8$GPa and $\nu = 0.25$ and plane strain conditions are assumed. The target error is $\eta_{\mathrm{t}} = 0.05$ for the adaptivity.

Adaptive steps can be seen in Fig. 11, where particles are added automatically around the crack tip and refinements are recovered when the crack tip propagates away. The final crack path can be seen in Fig. 12 for three cases. The results show that the difference of crack growth prediction through different initial particle arrangements is negligible and all agree with results from [26].

5.3. Cross crack

A cross crack in a square plate under biaxial loading is next considered. The geometry of this problem is given in Fig. 13 with $w = 20$mm and $w/h = 1$. The initial crack length is set to $a/w = 0.1$ and this ratio increases to 0.9 after the crack propagates. The biaxial tensile loading is $\sigma = 100$N/mm and the left bottom corner is totally fixed to constrain the plate. The target error $\eta_t = 0.06$ for the adaptivity is applied. Since this problem is symmetric, SIFs at the four crack tips are nearly the same, and the mode II SIF is negligible.

Adaptive results are presented in Fig. 14 for this problem with initial particle arrangements as in Fig. 15 (a). In Fig. 14 (a) the normalized global errors in Eq. (20) are obtained and it can be seen that the convergence rate using the adaptive refinement is much higher than for uniform refinement, and a converged value of the normalized K_I can be obtained from Fig. 14 (b). Due to the use of adaptivity, particle arrangements change during the crack propagation process, as shown in Fig. 15, and the number of nodes increases from 112 to 1851. Similar particle arrangements can be found at all four crack tips due to the problem's symmetry. Four "masses" of nodes are generated automatically and travel with the crack tips during crack propagation steps. Crack opening of the final step is shown in Fig. 16. Mode I SIFs at one crack tip for different crack lengths are compared with Daux et al. [17] and good agreement can be seen from Fig. 17.

5.4. Star shaped crack

The star shaped crack is more complicated than the cross crack, with an increase in crack tip number from 4 to 6. The geometry of this problem is shown in Fig. 18 with $w = 20$mm and $w/h = 1$. The crack length is initially $a/w = 0.1$ and increases to 0.9 after 8 crack propagation steps. The external loading is the same as the cross crack, with $\sigma = 100$N/mm, and for the adaptivity $\eta_t = 0.06$.

For this problem two sets of results are presented: firstly cracks are allowed to propagate but are constrained to maintain the same direction. In the second set of analyses this constraint is removed. The purpose of this approach is so that comparisons can be made to the results from Daux et al. [17] where SIFs are calculated for this problem using different initial crack lengths and no propagation, these being compared to the first set above. For the second set we include these to show that with propagation there is very little deviation from the straight crack paths anyway.

Firstly, node arrangements during the adaptive steps are shown in Fig. 19 and the maximum number of nodes generated during this process is 2158. Six "masses" of nodes can be seen around six crack tips and all travel with the crack tip during the crack propagation steps. Node distributions at two horizontal crack tips are symmetric while the situations at other crack tips are different, but the difference is small. Comparing the calculated SIFs at crack tips A and B, as in Fig. 20, all show good agreement with Daux et al. [17].

In contrast for the second set, the propagating angle is not constrained, and crack paths are not kept straight after crack propagation. Node arrangements are shown in Fig. 21 and it can be seen that node distributions around the two horizontal cracks are no longer symmetric. The maximum number of nodes becomes 2957. The calculated crack paths are depicted in Fig. 22, from which it can be seen that cracking angles of all 6 cracks keep constant at the beginning and then change a little at the last few steps. This is because the K_{II} of both crack tips A and B are tiny compared with K_{I} as shown in Fig. 20, so the deformations of all cracks are mainly of mode I type and the changes of all six crack directions are small.

5.5. Tree shaped crack

The final example is the most complex where a "tree" shaped crack with ten crack tips is considered. The geometry of this problem is presented in Fig. 23, with $w = 6$mm and $w/h = 1$, as in [27]. The cracks are defined by $a = b = 2c = 1$mm and $\alpha = 45°$, $\beta = 90°$. A biaxial tensile loading is applied, $\sigma = 100$N/mm. During the adaptivity, the target error is $\eta_{\mathrm{t}} = 0.06$.

The initial node arrangements are shown in Fig. 24 (a) and adaptive steps are presented in Figs. 24 (b) to (d). There are node refinements around the crack tips on both the left and right sides while refinements for the other six crack tips are not required. The number of nodes changes from 262 to 848. Extracting the SIFs of crack tips A, B, C and D in Fig. 23, convergent values can be obtained during adaptive steps (Fig. 25), where the superscripts on SIFs are used to indicate the crack tip. Good agreement is obtained when compared with results in [27], except for minor differences for K_{II} at crack tip A. K_{II} at crack tip A is near to 0 and the deformation is mainly of mode I type. Both K_{I} and K_{II} SIFs at crack tips B and C are small compared with crack tips A and D. This may explain why there are high levels of refinements around crack tips A and D but low levels for crack tips B and C it is low.

This tree shaped crack problem is more challenging if it starts from the edge, and we consider this crack problem in a double cantilever beam. The geometry of the problem is $w = 24$mm and $w/h = 3$. The crack pattern is not changed, with $a = b = 2c = 1$mm and $\alpha = 45°$, $\beta = 90°$. The right side of beam is fully fixed while the left side is under a pair of tractions with $\sigma = 100$N/mm, as shown in Fig. 26.

Adaptive steps are illustrated in Fig. 27 with initial node arrangements in Fig. 27 (a). There are refinements generated automatically around all 10 crack tips while the right part of beam is not influenced. The final number of nodes is 3359, 11 times larger than the initial value of 283. The crack opening is depicted in Fig. 28 (a) and an enlarged view of the rectangular zone is shown in Fig. 28 (b). The deformation of three cracks on the right is large. For the two branched cracks in the centre, only one part is open. The other two single cracks are not under large deformation. Checking the calculated SIFs at crack tips A, B, C and D as in Fig. 29, which are normalized by the same strategy as above, K_{I} values at crack tips A and D are nearly 3 times larger than the value at crack tip B while the K_{I} value at crack tip C is small. K_{II} at node A is 0 so the deformation of crack A is mainly of mode I type, similar

to crack tips B, C and D. This provides an explanation of why the deformations of cracks A and D are larger than crack B, while the opening of crack C is negligible. There are no other references which study this problem to our knowledge so it is difficult to make comparisons of accuracy regarding final SIFs, however the example demonstrates the potential power of this modified CPM and the adaptive scheme incorporated within it.

It is possible to use the proposed method to handle cases of crack coalescence, e.g. one crack growing into and splitting another, by introducing a particle at the intersection point and subsequently splitting it, but in this type of situation, when two crack tips are in close proximity, there will be difficulties in the evaluation of the J-integral which are not covered in this paper, so this aspect is not demonstrated here.

6. Conclusion

In this paper, a multiple-split modified cracking particle method is proposed for complex crack simulations in 2D. The discontinuity at a crack is fulfilled by splitting the cracking particles into several parts, and the crack opening at a location on the crack path can be simulated by relative displacements of these cracking particles. In this methodology, there is no need to use level set (or other) functions to describe discontinuities at crack paths and the expression of displacement approximation is kept simple. An adaptivity strategy has been used to control the number of nodes. Some multiple crack problems such as a cross crack, a star shaped crack and tree shaped cracks, have been tested to demonstrate the advantages of the proposed methodology and good agreement with previous results is obtained.

Acknowledgement

References

[1] W. Ai, C.E. Augarde, An adaptive cracking particle method for 2D crack propagation, Int. J. Numer. Methods Eng. 108 (2016) 1626–1648.

[2] M. Ambati, R. Kruse, L. De Lorenzis, A phase-field model for ductile fracture at finite strains and its experimental verification, Comput. Mech. 57 (2016) 149–167.

[3] X. An, G. Fu, G. Ma, A comparison between the NMM and the XFEM in discontinuity modeling, Int. J. Comput. Methods 9 (2012) 1240030.

[4] E. Barbieri, N. Petrinic, Three-dimensional crack propagation with distance-based discontinuous kernels in meshfree methods, Comput. Mech. 53 (2014) 325–342.

[5] E. Barbieri, N. Petrinic, M. Meo, V. Tagarielli, A new weight-function enrichment in meshless methods for multiple cracks in linear elasticity, Int. J. Numer. Methods Eng. 90 (2012) 177–195.

[6] T. Belytschko, T. Black, Elastic crack growth in finite elements with minimal remeshing, Int. J. Numer. Methods Eng. 45 (1999) 601–620.

[7] T. Belytschko, L. Gu, Y. Lu, Fracture and crack growth by element free Galerkin methods, Model. Simul. Mater. Sci. Eng. 2 (1994) 519–534.

[8] T. Belytschko, Y. Krongauz, D. Organ, M. Fleming, P. Krysl, Meshless methods: an overview and recent developments, Comput. Meth. Appl. Mech. Eng. 139 (1996) 3–47.

[9] T. Belytschko, Y. Lu, L. Gu, Element-free Galerkin methods, Int. J. Numer. Methods Eng. 37 (1994) 229–256.

[10] T. Belytschko, Y. Lu, L. Gu, Crack propagation by element-free Galerkin methods, Eng. Fract. Mech. 51 (1995) 295–315.

[11] T. Belytschko, Y. Lu, L. Gu, M. Tabbara, Element-free Galerkin methods for static and dynamic fracture, Int. J. Solids Struct. 32 (1995) 2547–2570.

[12] P.O. Bouchard, F. Bay, Y. Chastel, Numerical modelling of crack propagation: automatic remeshing and comparison of different criteria, Comput. Meth. Appl. Mech. Eng. 192 (2003) 3887–3908.

[13] E. Budyn, G. Zi, N. Moës, T. Belytschko, A method for multiple crack growth in brittle materials without remeshing, Int. J. Numer. Methods Eng. 61 (2004) 1741–1770.

[14] Y. Cai, J. Wu, S. Atluri, A new implementation of the numerical manifold method (NMM) for the modeling of non-collinear and intersecting cracks, Comp. Model. Eng. Sci. 92 (2013) 63–85.

[15] L. Chen, Y. Zhang, Dynamic fracture analysis using discrete cohesive crack method, Int. J. Numer. Meth. Biomed. 26 (2010) 1493–1502.

[16] H. Chung, T. Belytschko, An error estimate in the EFG method, Comput. Mech. 21 (1998) 91–100.

[17] C. Daux, N. Moes, J. Dolbow, N. Sukumar, T. Belytschko, Arbitrary branched and intersecting cracks with the extended finite element method, Int. J. Numer. Methods Eng. 48 (2000) 1741–1760.

[18] J. Dolbow, T. Belytschko, A finite element method for crack growth without remeshing, Int. J. Numer. Methods Eng. 46 (1999) 131–150.

[19] M. Duflot, A meshless method with enriched weight functions for three-dimensional crack propagation, Int. J. Numer. Methods Eng. 65 (2006) 1970–2006.

[20] T.P. Fries, M. Baydoun, Crack propagation with the extended finite element method and a hybrid explicit–implicit crack description, Int. J. Numer. Methods Eng. 89 (2012) 1527–1558.

[21] T.P. Fries, H.G. Matthies, Classification and Overview of Meshfree Methods, Institute of Scientific Computing, Technical University Braunschweig, Brunswick, Germany, 2004.

[22] A. Gravouil, N. Moës, T. Belytschko, Non-planar 3D crack growth by the extended finite element and level sets - part II: Level set update, Int. J. Numer. Methods Eng. 53 (2002) 2569–2586.

[23] V. Kumar, R. Drathi, A meshless cracking particles approach for ductile fracture, KSCE J. Civ. Eng. 18 (2014) 238–248.

[24] V. Kumar, A. Ghosh, Modeling of dynamic fracture based on the cracking particles method, Theor. Appl. Fract. Mech. 75 (2015) 22–31.

[25] V. Kumar, A. Ghosh, Non-linear dynamic fragmentation using cracking particles method, Comput. Mater. Sci. 98 (2015) 117–122.

[26] G. Lee, H. Chung, C. Choi, Adaptive crack propagation analysis with the element-free Galerkin method, Int. J. Numer. Methods Eng. 56 (2003) 331–350.

[27] G. Ma, X. An, H. Zhang, L. Li, Modeling complex crack problems using the numerical manifold method, Int. J. Fract. 156 (2009) 21–35.

[28] C. Miehe, M. Hofacker, F. Welschinger, A phase field model for rate-independent crack propagation: Robust algorithmic implementation based on operator splits, Comput. Meth. Appl. Mech. Eng. 199 (2010) 2765–2778.

[29] C. Miehe, F. Welschinger, M. Hofacker, Thermodynamically consistent phase-field models of fracture: Variational principles and multi-field fe implementations, Int. J. Numer. Methods Eng. 83 (2010) 1273–1311.

[30] B. Muravin, E. Turkel, Multiple crack weight for solution of multiple interacting cracks by meshless numerical methods, Int. J. Numer. Methods Eng. 67 (2006) 1146–1159.

[31] V.P. Nguyen, T. Rabczuk, S. Bordas, M. Duflot, Meshless methods: a review and computer implementation aspects, Math. Comput. Simul. 79 (2008) 763–813.

[32] D. Organ, M. Fleming, T. Terry, T. Belytschko, Continuous meshless approximations for nonconvex bodies by diffraction and transparency, Comput. Mech. 18 (1996) 225–235.

[33] M. Ortiz, A. Pandolfi, Finite-deformation irreversible cohesive elements for three-dimensional crack-propagation analysis, Int. J. Numer. Methods Eng. 44 (1999) 1267–1282.

[34] T. Rabczuk, T. Belytschko, An adaptive continuum/discrete crack approach for meshfree particle methods, Lat. Am. J. Solids Struct. 1 (2003) 141–166.

[35] T. Rabczuk, T. Belytschko, Cracking particles: a simplified meshfree method for arbitrary evolving cracks, Int. J. Numer. Methods Eng. 61 (2004) 2316–2343.

[36] T. Rabczuk, T. Belytschko, Adaptivity for structured meshfree particle methods in 2D and 3D, Int. J. Numer. Methods Eng. 63 (2005) 1559–1582.

[37] T. Rabczuk, T. Belytschko, Application of particle methods to static fracture of reinforced concrete structures, Int. J. Fract. 137 (2006) 19–49.

[38] T. Rabczuk, T. Belytschko, A three-dimensional large deformation meshfree method for arbitrary evolving cracks, Comput. Meth. Appl. Mech. Eng. 196 (2007) 2777–2799.

[39] T. Rabczuk, G. Zi, S. Bordas, H. Nguyen-Xuan, A simple and robust three-dimensional cracking-particle method without enrichment, Comput. Meth. Appl. Mech. Eng. 199 (2010) 2437–2455.

[40] G.H. Shi, Discontinuous deformation analysis: a new numerical model for the statics and dynamics of deformable block structures, Eng. Comput. 9 (1992) 157–168.

[41] I. Singh, B. Mishra, M. Pant, A modified intrinsic enriched element free Galerkin method for multiple cracks simulation, Mater. Des. 31 (2010) 628–632.

[42] Z. Ullah, C. Augarde, Finite deformation elasto-plastic modelling using an adaptive meshless method, Comput. Struct. 118 (2013) 39–52.

[43] H. Westergaard, Bearing pressures and cracks, J. Appl. Mech. 18 (1939).

[44] Z.A. Wilson, C.M. Landis, Phase-field modeling of hydraulic fracture, J. Mech. Phys. Solids 96 (2016) 264–290.

[45] S. Xu, Stable cracking particles method based on stabilized nodal integration and updated lagrangian kernel, Math. Probl. Eng. article-ID 646514 (2014) 1–10.

[46] X. Xu, A. Needleman, Numerical simulations of dynamic crack growth along an interface, Int. J. Fract. 74 (1995) 289–324.

[47] J. Yau, S. Wang, H. Corten, A mixed-mode crack analysis of isotropic solids using conservation laws of elasticity, J. Appl. Mech. 47 (1980) 335–341.

[48] H. Zhang, L. Li, X. An, G. Ma, Numerical analysis of 2-D crack propagation problems using the numerical manifold method, Eng. Anal. Bound. Elem. 34 (2010) 41–50.

[49] Y. Zhang, Meshless modelling of crack growth with discrete rotating crack segments, Int. J. Mech. Mater. Des. 4 (2008) 71–77.

[50] X. Zhuang, C. Augarde, S. Bordas, Accurate fracture modelling using meshless methods, the visibility criterion and level sets: formulation and 2D modelling, Int. J. Numer. Methods Eng. 86 (2011) 249–268.

[51] X. Zhuang, C. Augarde, K. Mathisen, Fracture modeling using meshless methods and level sets in 3D: framework and modeling, Int. J. Numer. Methods Eng. 92 (2012) 969–998.

[52] O.C. Zienkiewicz, R.L. Taylor, The Finite Element Method, volume 3, McGraw-hill London, 1977.

○ Normal particle

● Cracking particle

(a)   (b)
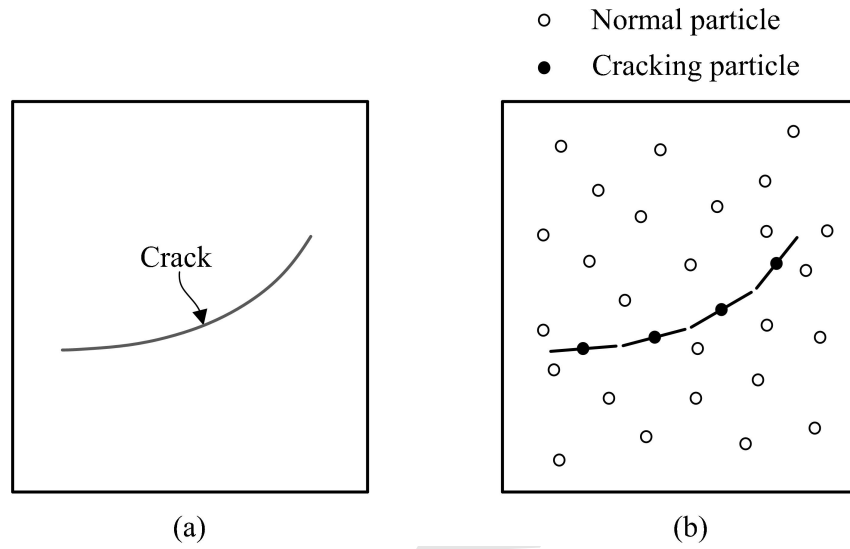
Figure 1: Crack description through the CPM.
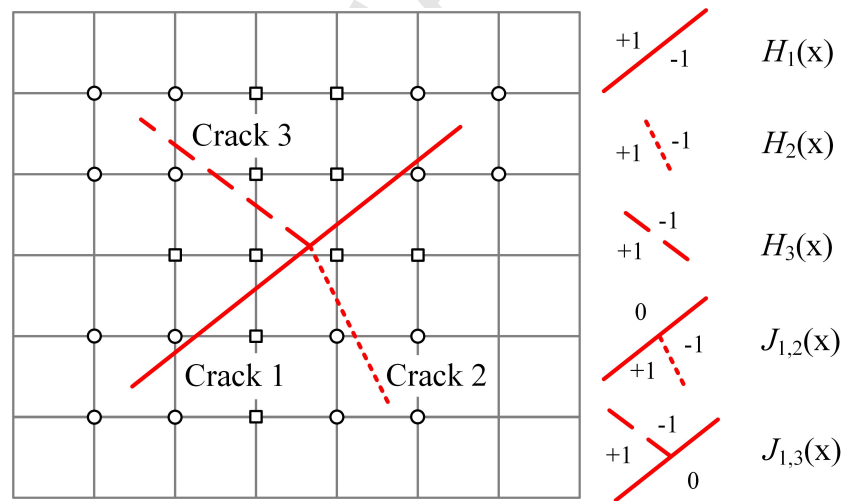
Figure 2: Sign functions in the XFEM for crack modelling.
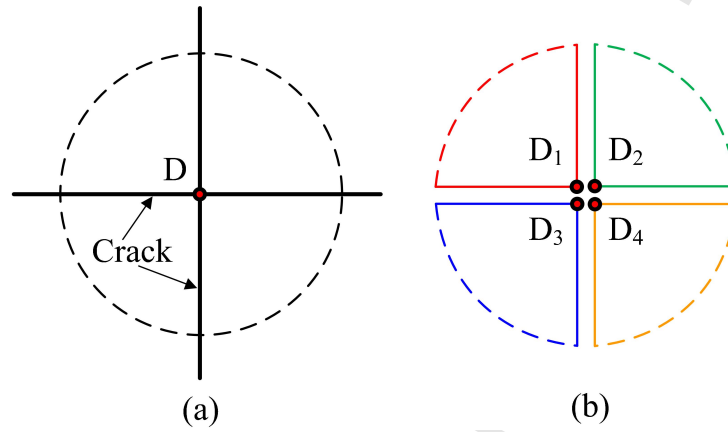
Figure 3: Multiple-split cracking particle.
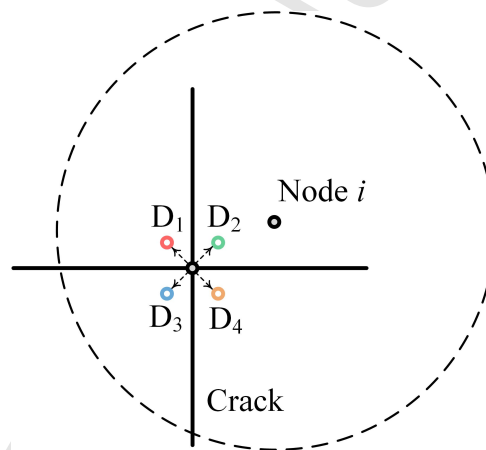
Figure 4: A simple strategy to distinguish cracking particles with the same location.
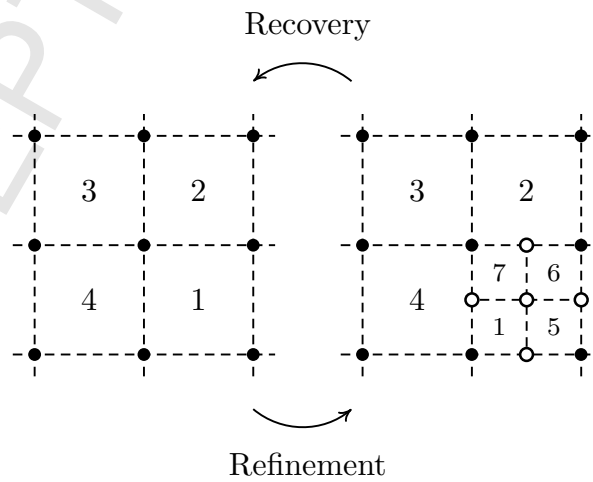
Figure 5: Adaptive procedure including the refinement and the recovery approaches.

19
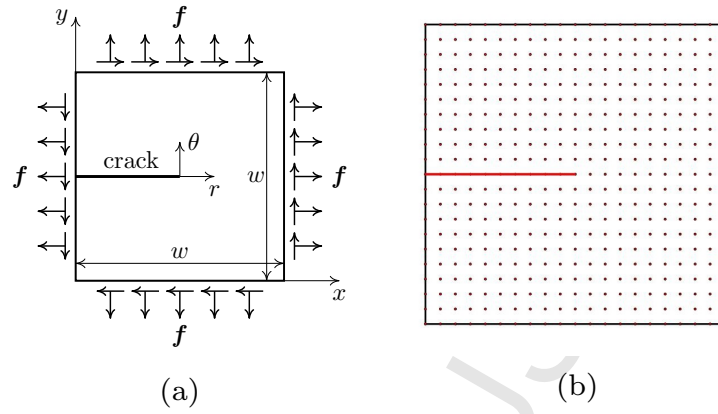
Figure 6: A near-tip field for a central crack in an infinite plate: (a) configuration; (b) initial particle arrangement.
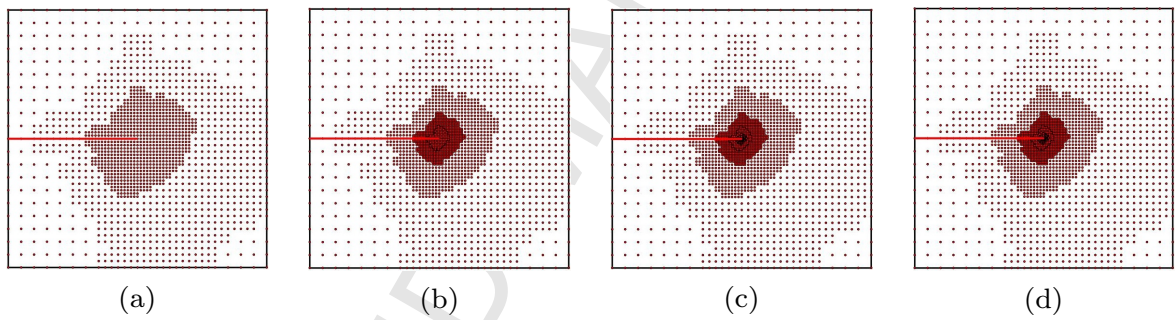
Figure 7: Adaptive particle distributions for a near-tip crack: (a) step 2; (b) step 4; (c) step 7; (d) step 9.
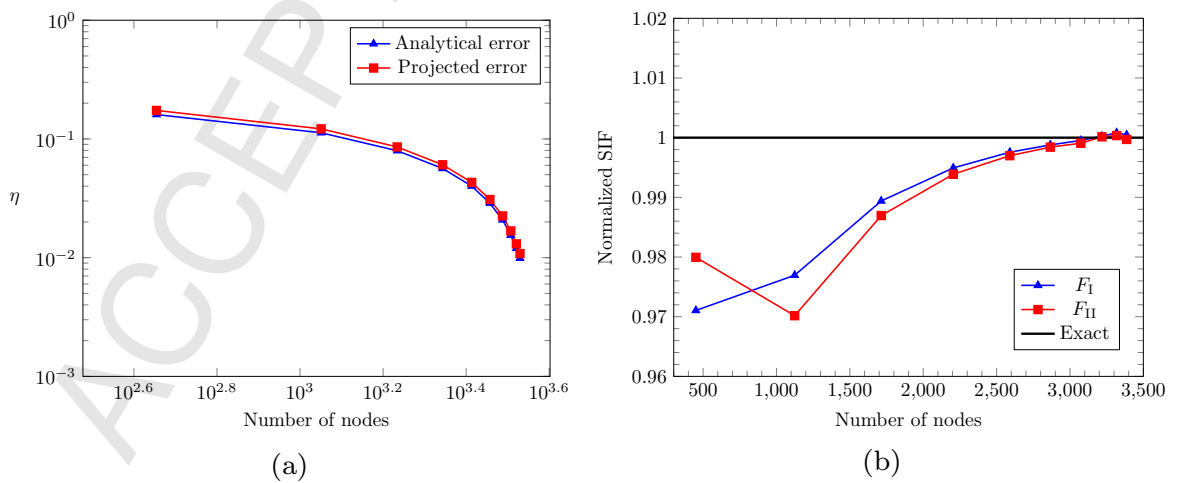
Figure 8: Adaptive results for a near-tip crack: (a) error estimation; (b) SIFs.

20
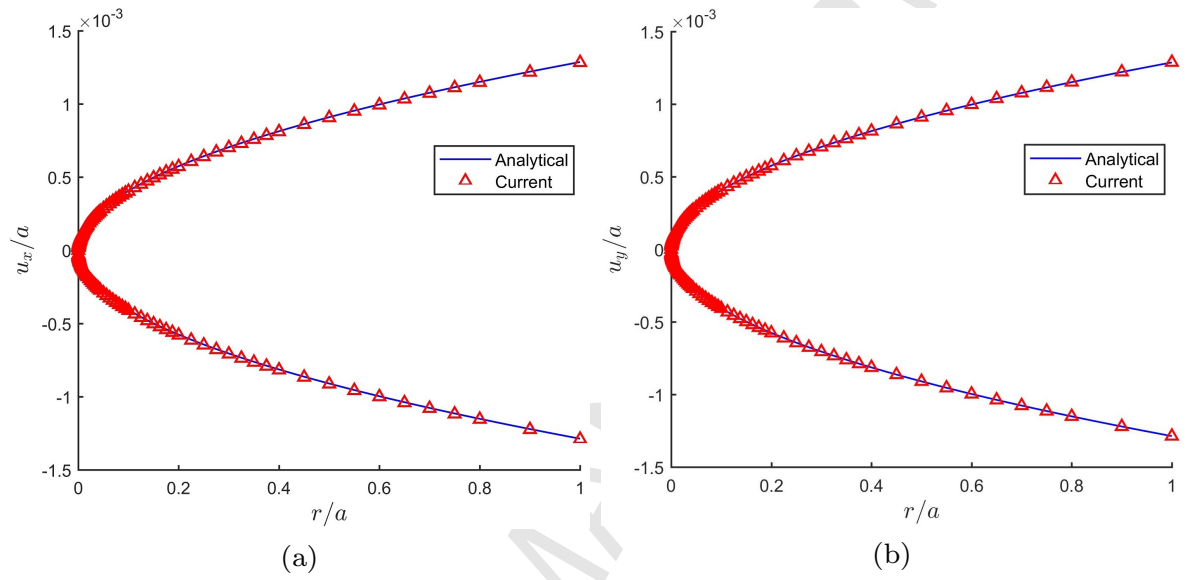
Figure 9: Final displacement for a near-tip crack: (a) u_x; (b) u_y.

Node arrangements	Adaptive		Uniform refinement			
	initial 20*20	20*20	60*60	100*100	200*200	300*300
Time/t_0	28.539	1.000	4.755	12.890	68.773	224.550
Analytical error	0.00989	0.16039	0.09185	0.07103	0.05017	0.04095
Projected error	0.01083	0.17385	0.09886	0.07633	0.05385	0.04393
Error (K_{I})	0.00048	0.02895	0.01216	0.00775	0.00399	0.00262
Error (K_{II})	0.00029	0.02005	0.01446	0.00932	0.00481	0.00314

Table 1: Comparison between adaptivity and uniform refinement for the near-tip crack problem.
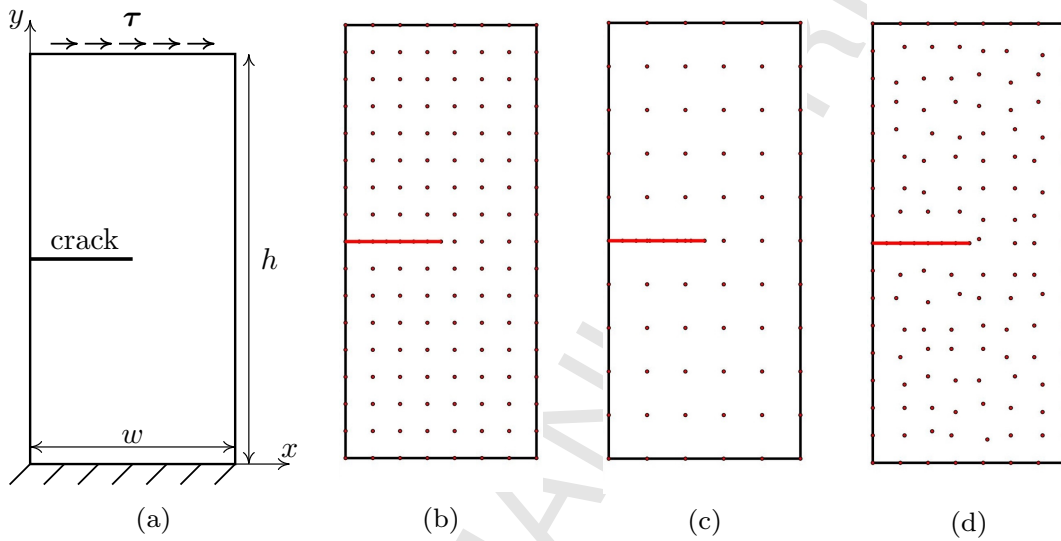
Figure 10: An edge crack under traction on the top with different particle arrangements: (a) configuration; (b) case 1; (c) case 2; (d) case 3.
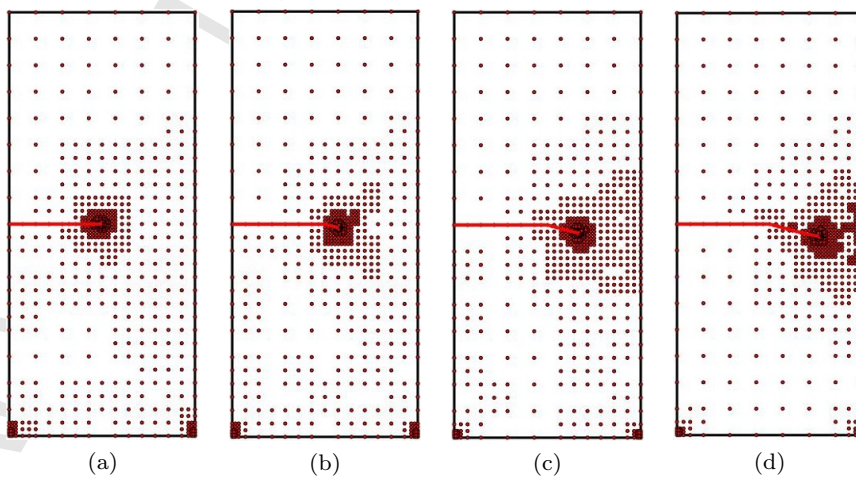
Figure 11: Crack propagation steps of an edge crack for case 1: (a) step 1; (b) step 4; (c) step 8; (d) step 12.
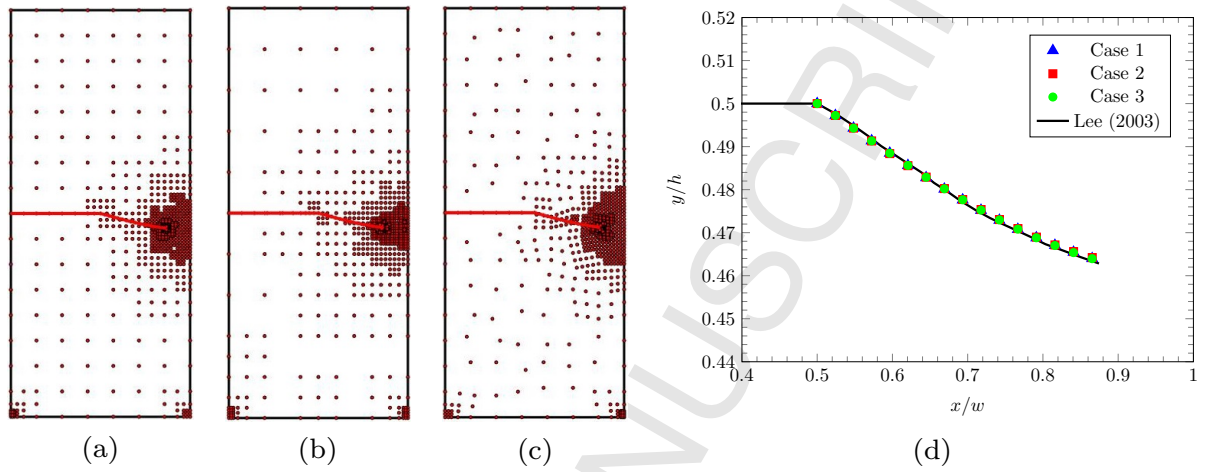
Figure 12: Predicted crack growth of an edge crack with different initial particle arrangements: (a) case 1; (b) case 2; (c) case 3; (d) comparison.
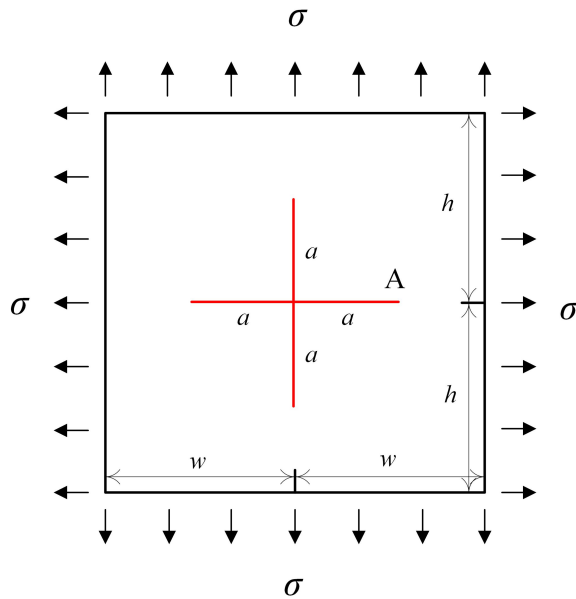
Figure 13: Configuration of the cross crack.
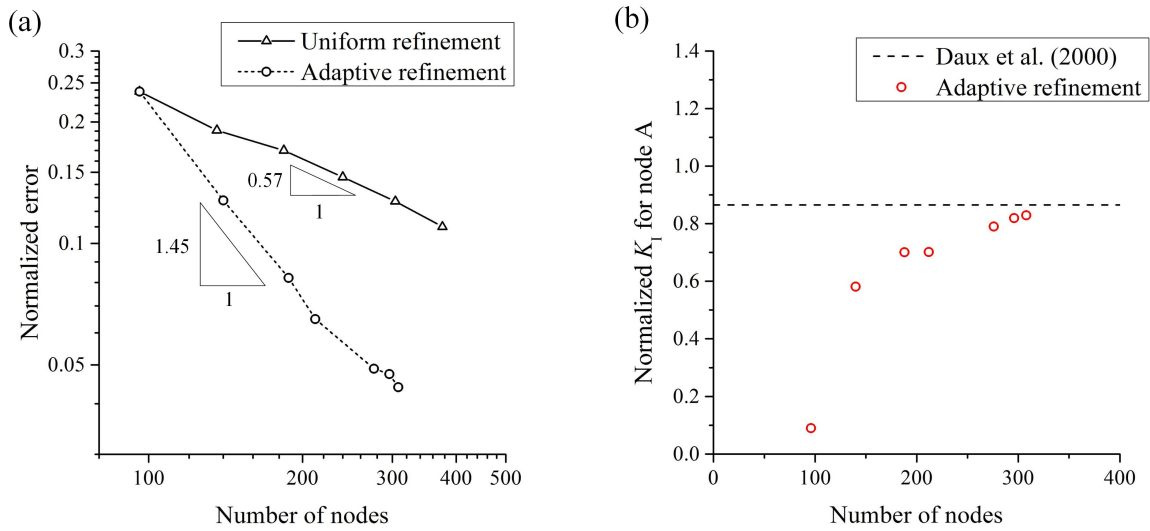
Figure 14: Adaptive results for initial cross crack: (a) error estimation; (b) normalized K_{I}.
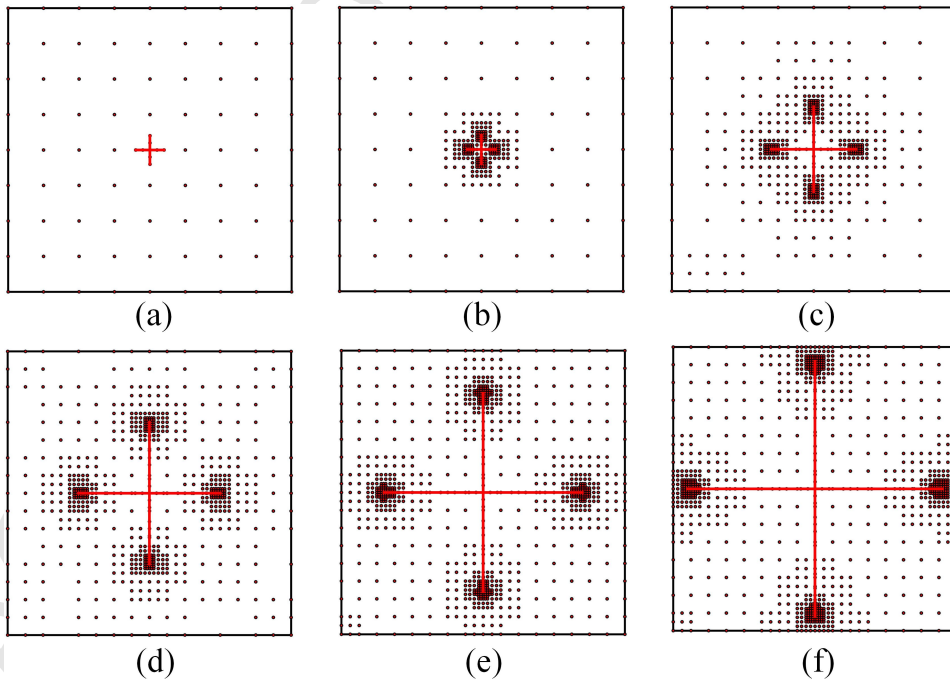
Figure 15: Adaptive steps for the cross crack with crack propagation: (a) initial nodes; (b) step 1; (c) step 3; (d) step 5; (e) step 7; (f) step 9.

24
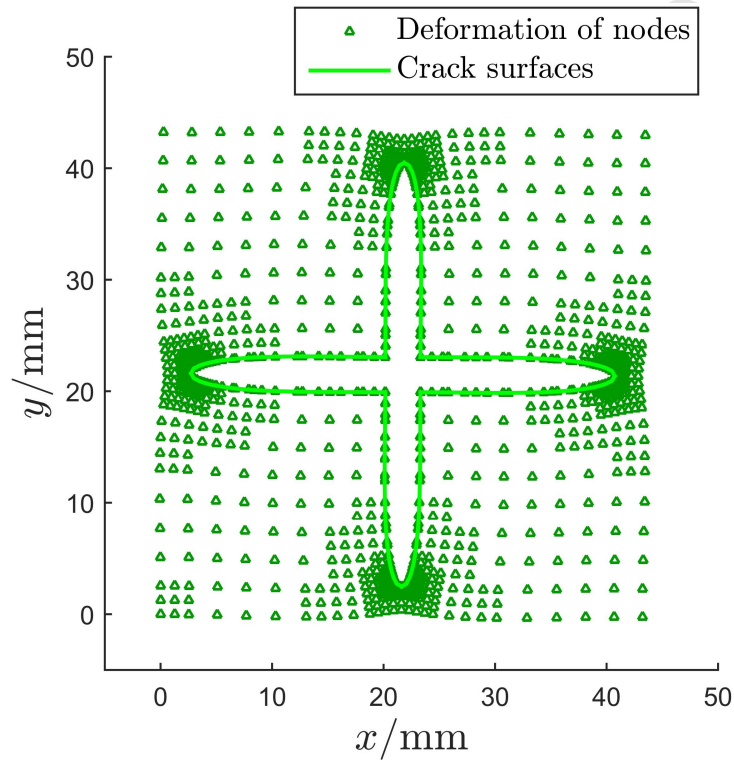
Figure 16: Final crack opening of the cross crack enlarged by 50 times.
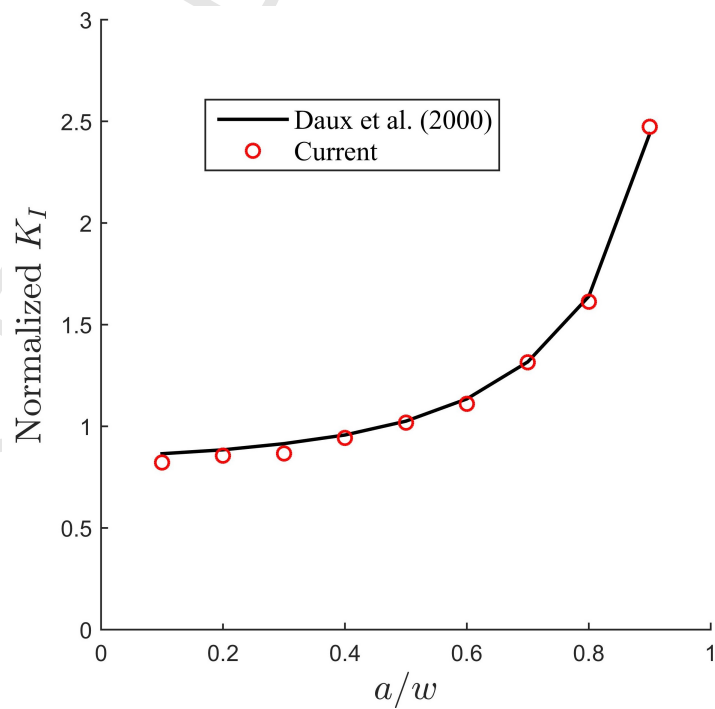
Figure 17: Normalized K_{I} at one crack tip of the cross crack during crack propagation.
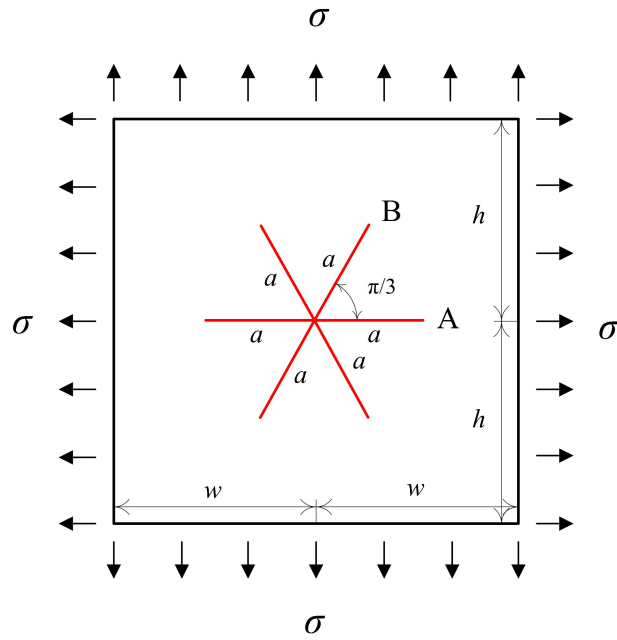
Figure 18: Configuration of the star shaped crack.
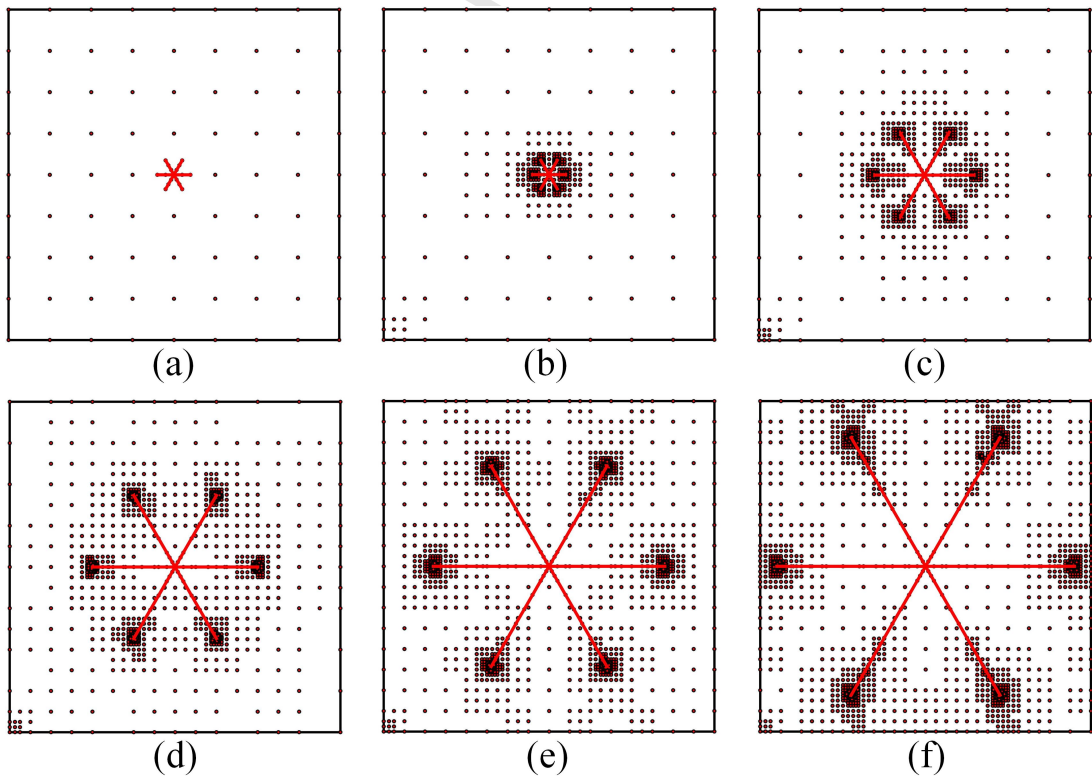
Figure 19: Adaptive steps for star shaped crack propagation without angular change: (a) initial nodes; (b) step 1; (c) step 3; (d) step 5; (e) step 7; (f) step 9.

26
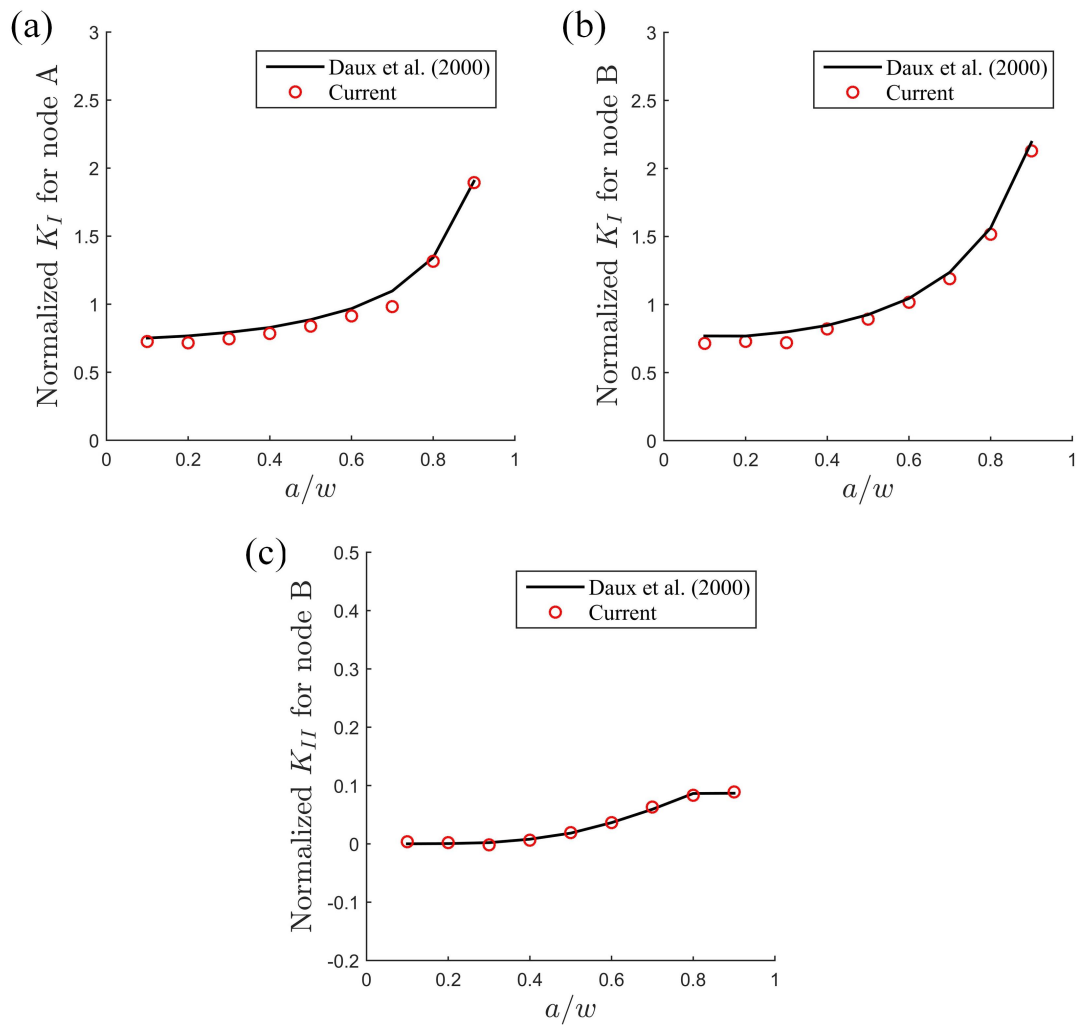
Figure 20: Verification of SIFs for the star shaped crack: (a) K_{I} at crack tip A; (b) K_{I} at crack tip B; (c) K_{II} at crack tip B.
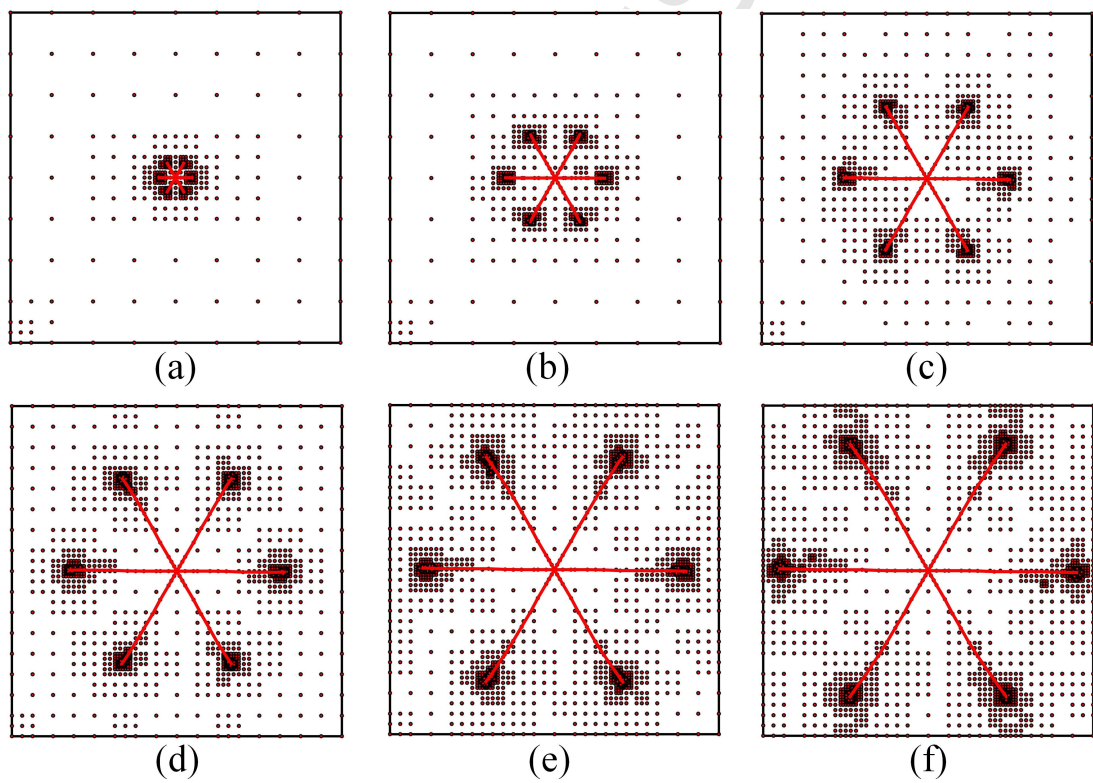
Figure 21: Adaptive steps for star shaped crack propagation with angular change: (a) step 1; (b) step 3; (c) step 5; (d) step 7; (e) step 9; (f) step 10.
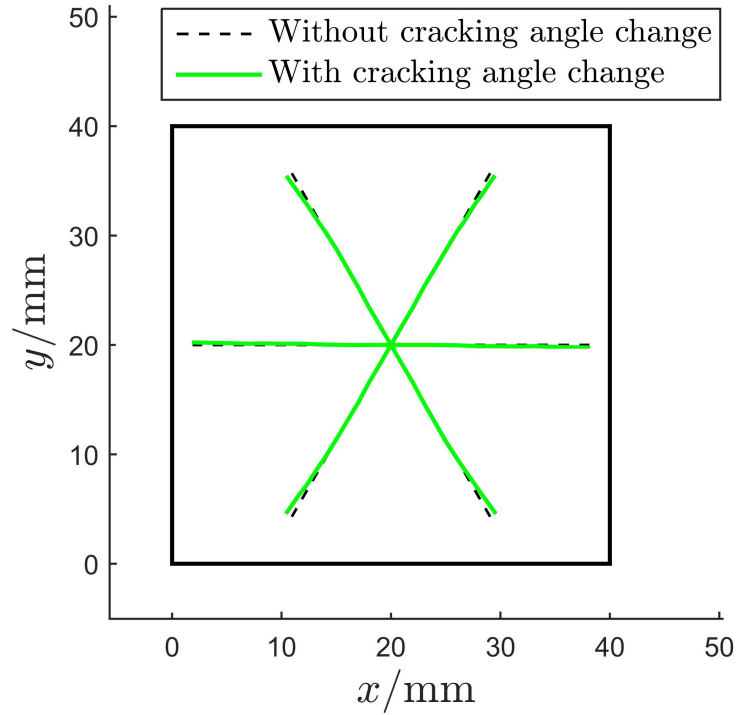
Figure 22: Comparison of crack path between with and without cracking angle change.
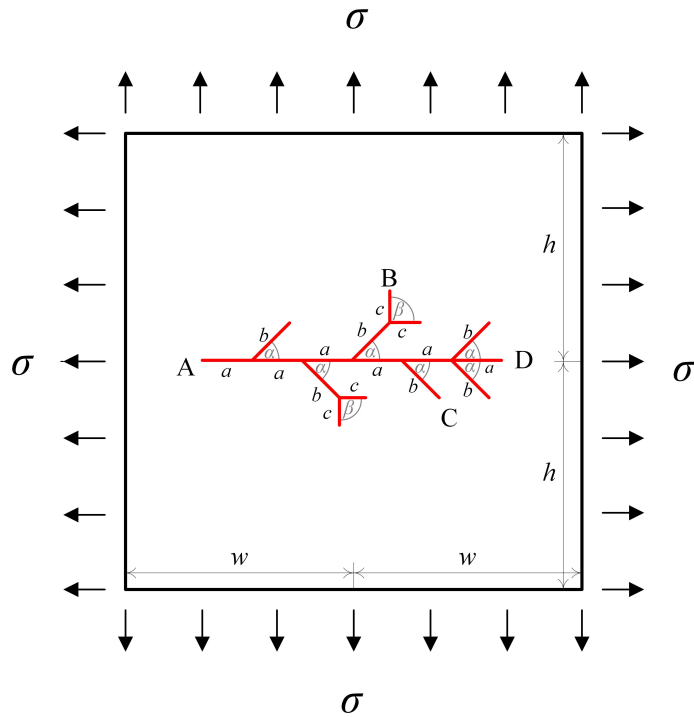
Figure 23: Configuration of the tree shaped crack in a square plate.

29
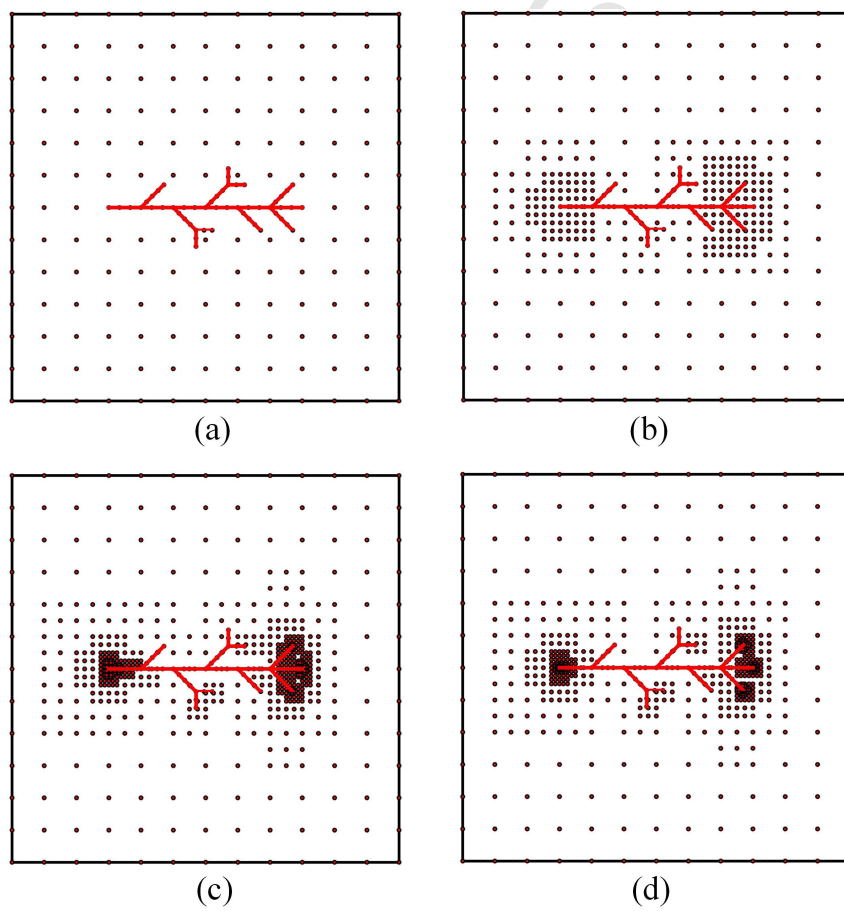
Figure 24: Adaptive steps for the tree shaped crack problem: (a) initial nodes; (b) step 2; (c) step 4; (d) step 6.
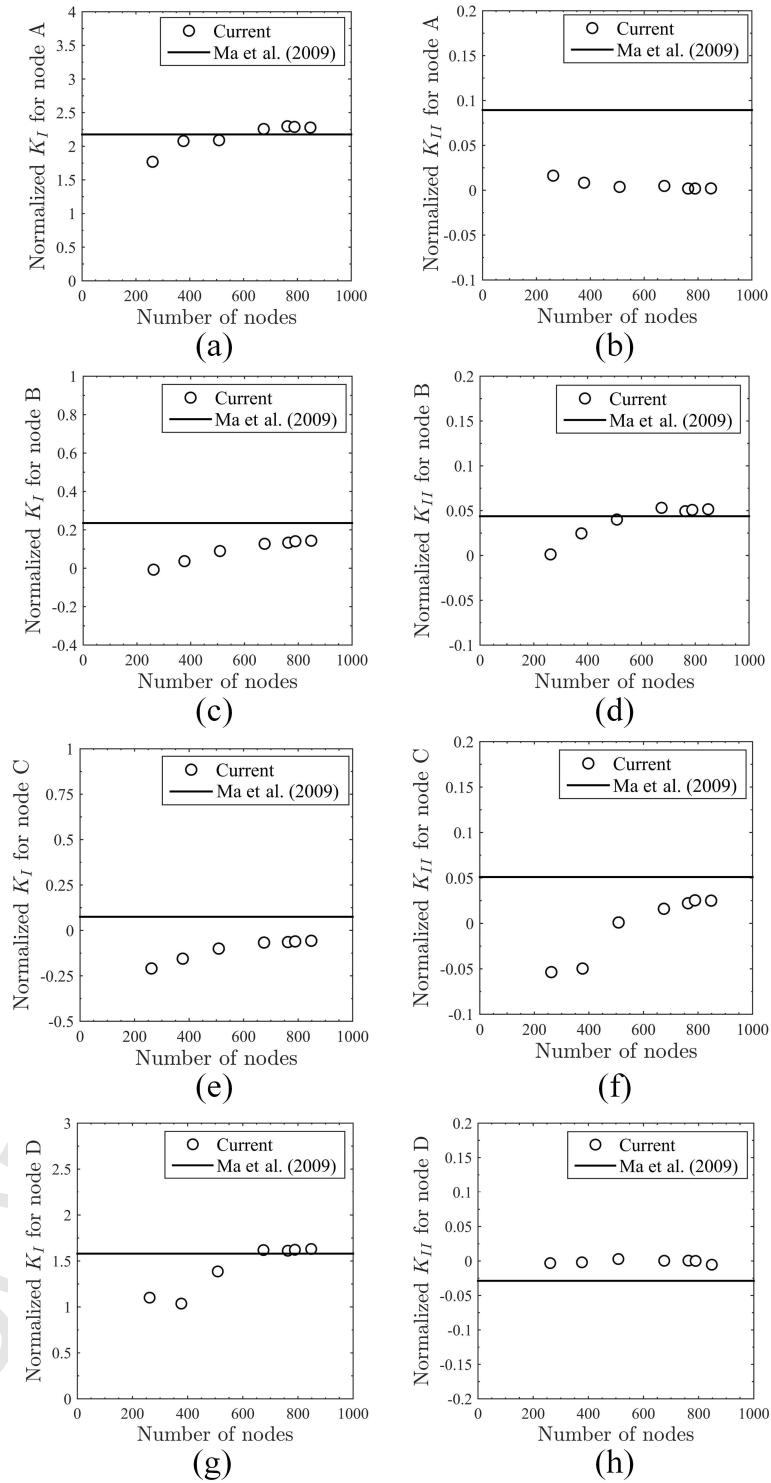
Figure 25: Verification of SIFs for the tree shaped crack problem: (a) F_I^A; (b) F_{II}^A (c) F_I^B; (d) F_{II}^B; (e) F_I^C; (f) F_{II}^C; (g) F_I^D; (h) F_{II}^D.
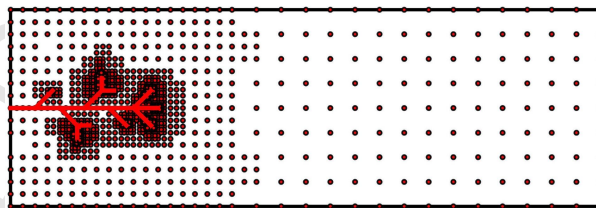
31
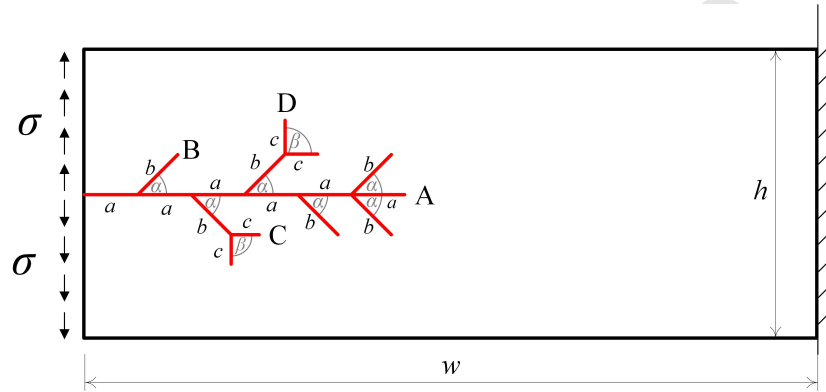
Figure 26: Configuration of tree shaped crack in a double cantilever beam.
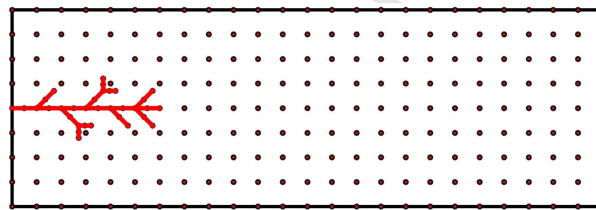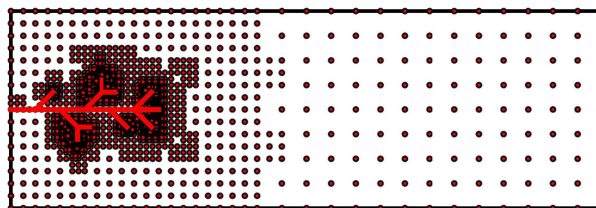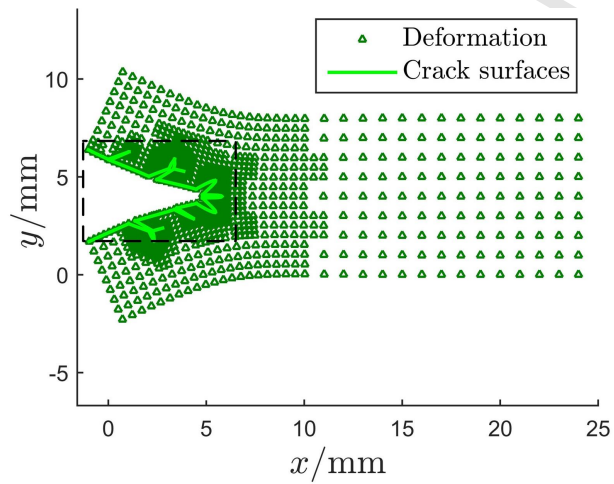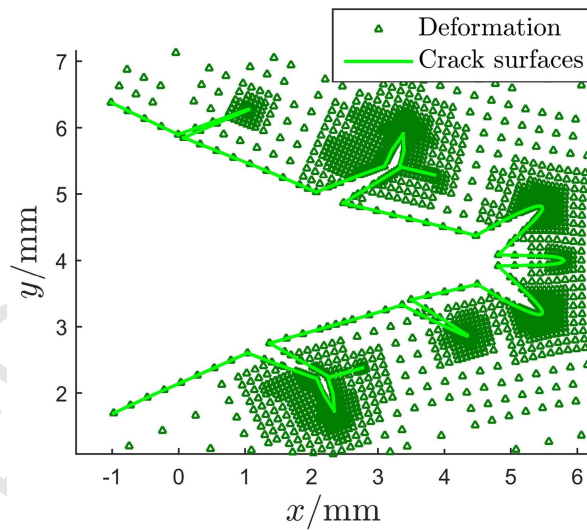

(a)
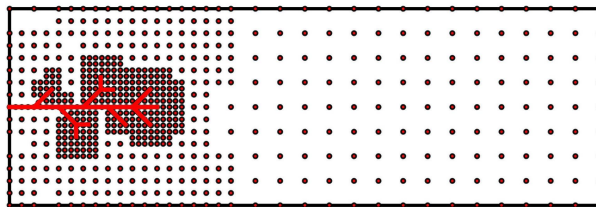
(b)

(c)

(d)

Figure 27: Adaptive steps for tree shaped crack in a double cantilever beam: (a) initial nodes; (b) step 2; (c) step 4; (d) step 6.

(a)

(b)

Figure 28: Crack opening for the tree shaped crack in a double cantilever beam enlarged by 20 times: (a) overall deformation; (b) partial enlarged view.
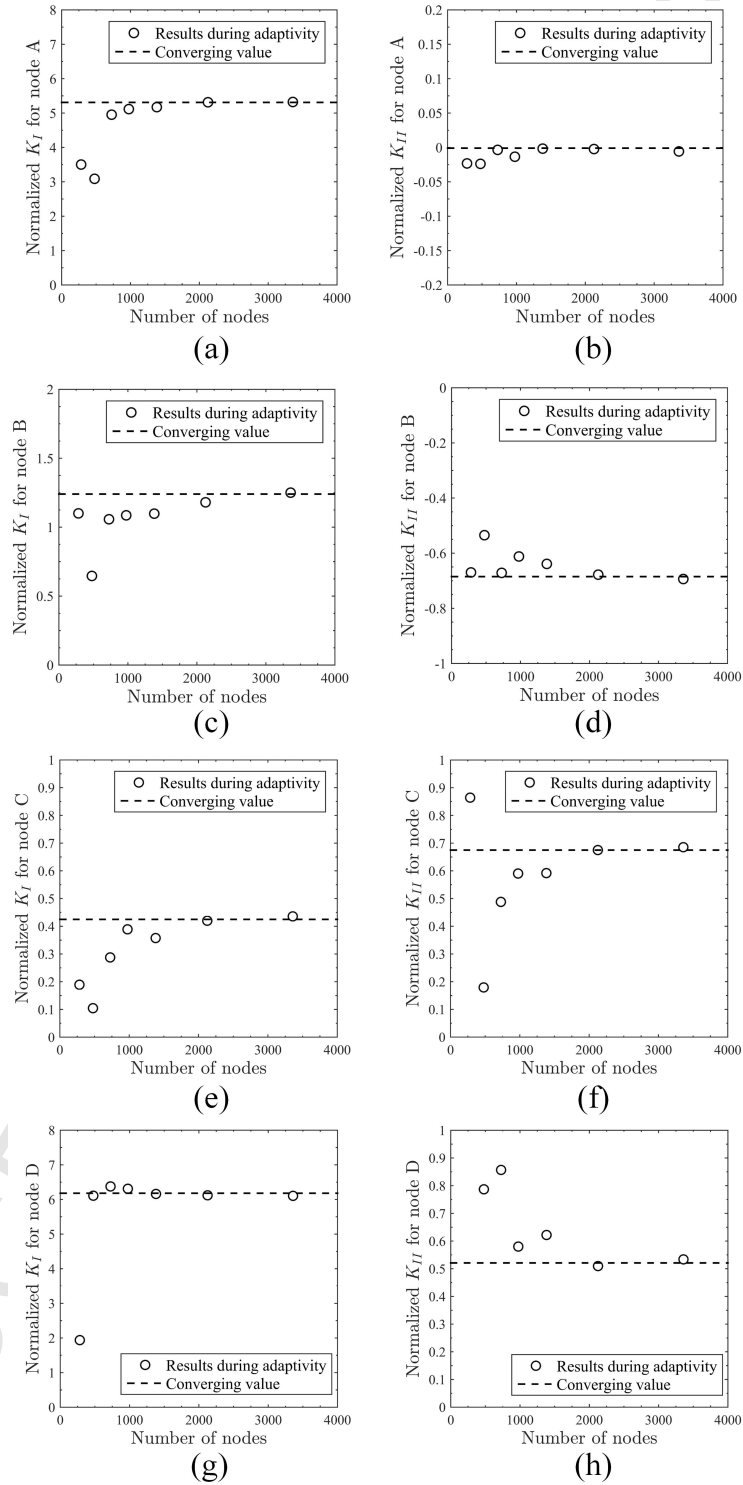
33

Figure 29: Calculated SIFs for the tree shaped crack in a double cantilever beam: (a) $F_{\mathrm{I}}^{\mathrm{A}}$; (b) $F_{\mathrm{II}}^{\mathrm{A}}$ (c) $F_{\mathrm{I}}^{\mathrm{B}}$; (d) $F_{\mathrm{II}}^{\mathrm{B}}$; (e) $F_{\mathrm{I}}^{\mathrm{C}}$; (f) $F_{\mathrm{II}}^{\mathrm{C}}$; (g) $F_{\mathrm{I}}^{\mathrm{D}}$; (h) $F_{\mathrm{II}}^{\mathrm{D}}$

Highlights for paper "A Multi-Cracked Particle Method for Complex Fracture Problems"

- A Multi-Cracked Particle Method is presented, which can provide a simple way to handle crack branches and crack junctions.
- Adaptivity is introduced to improve the calculating efficiency.
- Fracture problems with up to ten crack tips are considered and good results are obtained, which shows the performance of this methodology.